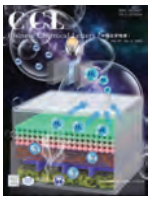
Chinese Chemical Letters 37 (2026) 111433

Contents lists available at ScienceDirect

Chinese Chemical Letters

journal homepage: www.elsevier.com/locate/cclet



Nanoemulsion-assisted assembly and polymerization towards core-shell magnetic mesoporous melamine-formaldehyde resin microspheres

Jiarong Li[a], Shude Liu[a], Yuanzhao Xie[a], Yue Sun[a], Zhuyu Liu[a], Meihua Chen[a,*], Yaobang Li[b,*], Yonghui Deng[a,*]

[a] *Department of Chemistry, Shanghai Stomatological Hospital & School of Stomatology, State Key Laboratory of Coatings for Advanced Equipment, Shanghai Key Laboratory of Molecular Catalysis and Innovative Materials, College of Smart Materials and Future Energy, Fudan University, Shanghai 200433, China*
[b] *Zhejiang Fulai New Materials, Co., Ltd., Jiaxing 314103, China*

ARTICLE INFO

Article history:
Received 27 April 2025
Revised 3 June 2025
Accepted 10 June 2025
Available online 10 June 2025

Keywords:
Core-shell structure
Magnetic mesoporous materials
Melamine-formaldehyde resin
Esterification catalysis
Antibacterial materials

ABSTRACT

Core-shell magnetic polymer microspheres with mesoporous organic shells hold immense potential in diverse applications, encompassing adsorption, separation, delivery/immobilization of guest molecules in catalysis and controlled drug release. Herein, magnetic mesoporous melamine-formaldehyde resin microspheres (Fe_3O_4@SiO_2@mMF) are constructed *via* a nanoemulsion-assisted interfacial co-assembly and polymerization strategy, using Pluronic F127 as a template agent and soluble melamine-formaldehyde (MF) oligomer as the precursor. The resulting microspheres possess radially oriented mesopores, superparamagnetic properties, and abundant N-containing active sites (nitrogen content: 15.02 wt%). The as-synthesized Fe_3O_4@SiO_2@mMF microspheres as ideal catalyst supports, exhibit exceptional loading capacity for phosphotungstic acid (PTA). The as-formed Fe_3O_4@SiO_2@mMF/PTA composites demonstrate not only good catalytic performance in the esterification reaction of *n*-butanol and acetic acid with a high conversion of 92 % (to acetic acid) but also excellent antimicrobial performance against Staphylococcus aureus and *Escherichia coli* with viabilities of 11.58 % and 7.35 %, respectively.

© 2026 Published by Elsevier B.V. on behalf of Chinese Chemical Society and Institute of Materia Medica, Chinese Academy of Medical Sciences.

Ordered mesoporous materials have attracted extensive research interest in the realm of porous materials due to their high specific surface area, ordered pore structures, uniform pore sizes, tunable composition, and easily modifiable surface [1–4]. These materials are garnering significant attention across diverse application fields, including catalysis [5,6], biosensing [7,8], gas sensing [9,10], drug delivery [11–13], and energy storage [14,15]. The synthesis of mesoporous materials predominantly employs the soft templating method [16–18], and ionic surfactants like cetyltrimethylammonium bromide (CTAB) and non-ionic surfactants like Pluronic F127 were used to act as the structure-directing agent for generation of mesoporous materials with diverse framework compositions such as silica [19–22], organic polymers [23,24], and carbon [25–27]. To endow mesoporous materials with more functionalities, considerable efforts have recently been made to integrate mesoporous materials with other functional nanomaterials such as graphene [28–30], carbon nanotubes [31,32], Au nanoparticles [33,34], quantum dots [35,36] and other functional nanoparticles or nanocrystals [37,38] *via* different synthesis methods. The combination of magnetic nanoparticles and mesoporous materials has garnered particular interest [39–41]. Magnetic material with favorable magnetic responsiveness enables the recovery and accurate positioning of guest objects immobilized on magnetic materials *via* an external magnetic field [42,43]. This property underscores the strategic advantage of developing magnetically responsive mesoporous materials, which not only retains the intrinsic benefits of mesoporous structures but also offers unprecedented control over material positioning and retrievability [44–47]. Magnetic mesoporous materials have multifunctional advantages in various applications by using the synergy of porosity and magnetism for sustainable catalysis, precision medicine, and environmental management. However, constructing such architectures presents significant challenges: (1) Maintaining structural integrity during magnetic core encapsulation often compromises pore accessibility; (2) Preventing magnetic nanoparticle aggregation under reaction conditions while preserving mesopore uniformity requires delicate synthetic control; (3) Achieving strong interfacial interac-

* Corresponding authors.
E-mail addresses: chenmeihua@fudan.edu.cn (M. Chen), yaobangli@alleadprint.com (Y. Li), yhdeng@fudan.edu.cn (Y. Deng).

https://doi.org/10.1016/j.cclet.2025.111433
1001-8417/© 2026 Published by Elsevier B.V. on behalf of Chinese Chemical Society and Institute of Materia Medica, Chinese Academy of Medical Sciences.

tions between magnetic cores and porous shells to prevent catalytic component leaching remains non-trivial.

Most previously reported magnetic mesoporous materials are based on core-shell structures with magnetic iron oxide (*e.g.*, magnetite) core and mesoporous silica shell, and in practical applications, the pore walls of mesoporous silica shell can be modified by silane chemistry to facilitate their applications such as loading drug molecules [48,49], immobilization of catalysts [50,51], selective adsorption and separation [52]. Nevertheless, the tedious surface functionalization processes and limited functional group coverage hinder their broader applications. Recently, constructing the mesoporous polymer shell on colloidal functional cores has been an efficient approach to developing mesoporous microspheres with rich functional groups or high density of active sites. For instance, by directly coating mesoporous resin shells over Fe_3O_4 particles *via* interface assembly and polymerization strategy, the microspheres with superparamagnetism and abundant adsorption sites could be fabricated for adsorption and heterogeneous catalysis [53,54]. Similarly, using colloidal Au nanoparticles as the core and mesoporous polydopamine as the shell, the microspheres with the photothermal properties and high loading capacity endow the significant potential in cell tracing and targeted drug release [55]. In addition, the synergetic integration of nanozymes cores (*e.g.*, colloidal Cu, precious metals) and bio-enzyme-immobilized mesoporous shells have demonstrated enhanced cascade reaction activity for conversion and antibacterial [56,57]. Despite these progresses, the controllable synthesis of core-shell magnetic polymer microspheres with tunable pore size, abundant functional groups, and well-defined architectures remains challenging because the underlying formation mechanism and their wide application are yet to be explored.

In this study, core-shell magnetic mesoporous melamine-formaldehyde resin microspheres (Fe_3O_4@SiO_2@mMF) were constructed through a nanoemulsion-assisted interfacial assembly and polymerization strategy. The synthesis involves the co-assembly of F127 and melamine-formaldehyde (MF) precursor in the presence of pre-synthesized silica-coated magnetite (Fe_3O_4@SiO_2) colloidal particles in a nanoemulsion solution. The obtained Fe_3O_4@SiO_2@mMF microspheres exhibit distinct characteristics, including radially oriented mesopores, superparamagnetic responsiveness, and abundant nitrogen-containing active sites (nitrogen content 15.02 wt%). As smart carriers, Fe_3O_4@SiO_2@mMF microspheres demonstrate outstanding loading capacity for multifunctional phosphotungstic acid (PTA), and the synthesized Fe_3O_4@SiO_2@mMF/PTA catalyst displays remarkable catalytic performance in the esterification of butanol and acetic acid with a high conversion rate (92 %) and good recycling stability, while also exhibiting excellent antibacterial activity against *Staphylococcus aureus* (*S. aureus*) and *E. coli* (*E. coli*) with viabilities of 11.58 % and 7.35 %, respectively.

The synthesis of Fe_3O_4@SiO_2@mMF microspheres is depicted in Fig. 1. Firstly, uniform water-dispersible Fe_3O_4 particles synthesized *via* solvothermal reaction [58] were coated by a layer of dense silica *via* the sol-gel method [40]. The silica shell provides excellent biocompatibility and protection for the Fe_3O_4 core. Subsequently, MF oligomers prepared by heating at 100 °C for 30 min under alkaline conditions were used to assemble with F127 triblock copolymers in an acidic aqueous solution in the presence of colloidal Fe_3O_4@SiO_2 microspheres and 1,3,5-trimethylbenzene (TMB). During the synthesis, F127 and TMB co-assemble into uniform oil/water nano-emulsion consisting of monodispersed TMB-swelled F127 micelles, and the hydrophilic PEO segments of F127 micelles can interact with the MF oligomers which can undergo a further condensation to form mesostructured MF/F127/TMB composites on the colloidal Fe_3O_4@SiO_2 microspheres, thus forming Fe_3O_4@SiO_2@MF/F127 composite microspheres. After removing the

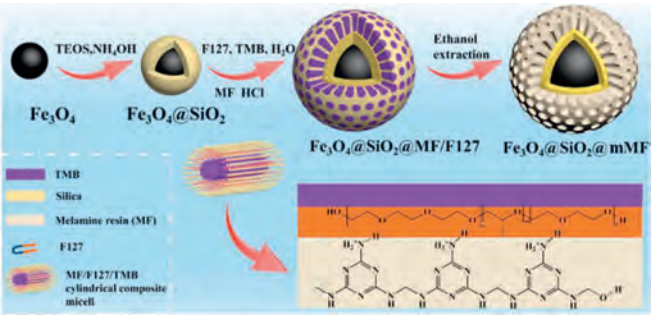


Fig. 1. Synthesis procedure for Fe_3O_4@SiO_2@mMF microspheres with radially aligned mesopore channels.

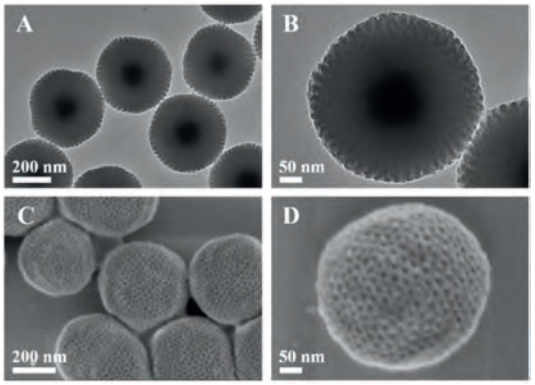


Fig. 2. (A, B) TEM and (C, D) SEM images of the as-synthesized Fe_3O_4@SiO_2@mMF microspheres.

template by ethanol extraction, Fe_3O_4@SiO_2@mMF microspheres with radial pores can finally be obtained.

The as-synthesized hydrophilic Fe_3O_4 particles exhibit a mean diameter of 80 nm and consist of 8.0 nm magnetic nanocrystals according to the transmission electron microscopy (TEM) observation (Fig. S1A in Supporting information). Uniform colloidal Fe_3O_4@SiO_2 microspheres with a diameter of 180 nm are obtained by coating a dense silica layer of 50 nm on magnetic particles *via* the sol-gel reaction (Fig. S1B in Supporting information). On the one hand, the dense silica shell can prevent the Fe_3O_4 core from oxidation and corrosion. On the other hand, the silica shell with rich silanol groups provides the high-density anchoring points, and therefore the microspheres can bind melamine resin precursor molecules through hydrogen bonding [59]. Meanwhile, F127/TMB micelles can interact with pre-synthesized soluble MF oligomers (see Experimental section in Supporting information) through the mediation of H^+ of the acidic catalyst. As a result, homogeneous MF/F127/TMB shells can deposit on the surface of Fe_3O_4@SiO_2 through interfacial assembly of F127/TMB micelles and condensation (*i.e.*, further polymerization) of MF oligomers. After removal of F127 and TMB *via* ethanol extraction, highly dispersed Fe_3O_4@SiO_2@mMF microspheres with a uniform diameter of 300 nm were obtained, corresponding to the porous MF shell of 60 nm (Fig. 2). They have a well-defined core-multishell structure and radially aligned pore channels. High-angle annular dark-field scanning transmission electron microscopy (HAADF-STEM), coupled with energy-dispersive X-ray spectroscopy (EDX), provided further information on the core-multishell structure and elemental composition (Fig. S2 in Supporting information). The EDX element mapping, presented as an overlay of Fe, Si, C, and N elements, confirmed the presence of distinct layers and a core-multishell configuration (Figs. S2C–H). Notably, the high content of nitrogen (N) element, with a mass fraction of 15.02 % (Fig. S2I) further validated

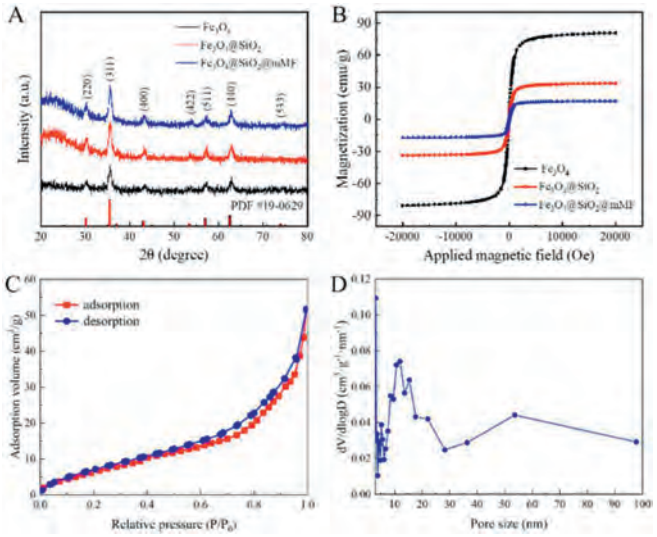


Fig. 3. (A) The wide-angle XRD pattern and (B) magnetic hysteresis loops of Fe_3O_4, Fe_3O_4@SiO_2 and Fe_3O_4@SiO_2@mMF microspheres. (C) N_2 adsorption-desorption isotherms and (D) pore size distribution of Fe_3O_4@SiO_2@mMF microspheres.

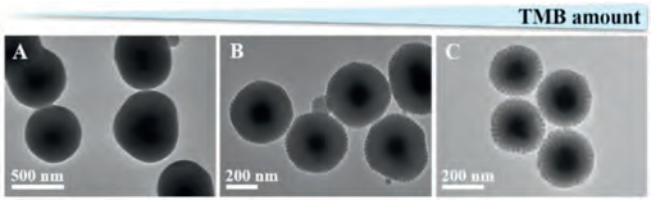


Fig. 4. TEM images of Fe_3O_4@SiO_2@mMF microspheres synthesized using different amount of TMB: (A) 0, (B) 0.6, (C) 1.2 mL.

the versatile interface multicomponent co-assembly and polymerization synthesis method.

X-ray photoelectron spectroscopy (XPS) characterization (Fig. S3 in Supporting information) indicates the existence of C, O, Si, and abundant N elements, which is in good agreement with the EDX results. The high-resolution profiles of C 1s show the distinct peaks of C=C (284.6 eV), C–O (286.3 eV), C=N (287.7 eV) and O-C=O (288.8 eV) bonds, respectively. The high-resolution profile of N 1s exhibits two prominent peaks at 398.3 and 399.8 eV, which can be attributed to pyridinic N and pyrrolic N, respectively. The wide-angle X-ray diffraction (XRD) patterns of the synthesized Fe_3O_4, Fe_3O_4@SiO_2, and Fe_3O_4@SiO_2@mMF samples (Fig. 3A) reveal broad peaks at 30.1°, 35.4°, 43.1°, 56.9° and 62.5°, which can be indexed to magnetite (JCPDS No. 19–0629). The characterization of magnetic property using the magnetic property measurement system (MPMS) indicates that both Fe_3O_4@SiO_2 and Fe_3O_4@SiO_2@mMF microspheres have superparamagnetism (Fig. 3B and Fig. S4 in Supporting information). However, the magnetization saturation values decrease from 40 emu/g for Fe_3O_4@SiO_2 to 20 emu/g for Fe_3O_4@SiO_2@mMF, attributed to the additional non-magnetic coatings of silica and mMF layers. The obtained Fe_3O_4@SiO_2@mMF microspheres can be rapidly dispersed and conveniently collected within tens of seconds using a neodymium (NdFeB) magnet (200 mT), demonstrating their excellent magnetic responsiveness. Nitrogen adsorption-desorption of the obtained Fe_3O_4@SiO_2@mMF (Fig. 3C) displays a *quasi*-type-IV isotherm with nitrogen capillary condensation occurring at a high relative pressure (P/P_0) range of 0.6–0.95 and a continuous nitrogen evaporation in the P/P_0 range of 0.75–0.85. The Brunauer-Emmett-Teller (BET) surface area was calculated to be 94 m^2/g, indicative of a high surface area considering the presence of the high-density iron oxide core. Furthermore, the pore size distribution (Fig. 3D), derived from the nitrogen adsorption branch according to the Barret-Joyner-Halenda (BJH) model, indicates a relatively uniform pore size of 11.4 nm, and such large mesopores are particularly favorable for loading or supporting guest objects in catalysis or separation. The pore of about 55.0 nm probably corresponds to the interstitial voids of the closely packed microspheres after drying.

It is noteworthy that the TMB concentration in the synthesis system containing colloidal Fe_3O_4@SiO_2, MF oligomer, and hydrochloric acid (HCl) catalyst, has a great influence on the formation of Fe_3O_4@SiO_2@mMF microspheres. In the absence of TMB, the colloidal Fe_3O_4@SiO_2 were encapsulated by a dense, nonporous resin layer after synthesis (Fig. 4A), because the F127 molecules failed to form large micellize that are capable of inducing the condensation of MF oligomers in the micelles' surface. Upon the introduction of an appropriate amount of TMB (Figs. 4B and C), the obtained core-shell microspheres exhibit radially divergent pore structure in the shell due to the favorable interfacial co-assembly process induced by TMB-swelled F127 micelles in the reaction system. The introduction of TMB enables the amphiphilic F127 to form stable F127/TMB spherical micelles in the oil-water mixture, *i.e.*, nanoemulsion. During the reaction, the PEO segments of F127 in the surface of the micelles can interact with the soluble MF oligomers *via* the mediation of H^+ ions and meanwhile the silane groups on the surface of colloidal Fe_3O_4@SiO_2 can interact with PEO of the F127/TMB micelles *via* hydrogen bond, and thus the polymerization/condensation of MF oligomer drives the assembly and formation of MF/F127/TMB composite mesostructure on the Fe_3O_4@SiO_2 colloids. After removing TMB and F127 *via* ethanol extraction, Fe_3O_4@SiO_2@mMF microspheres were finally obtained. Moreover, the silica shell is also important for the formation of well-defined Fe_3O_4@SiO_2@mMF composite microspheres. In this study, a similar synthesis was carried out using colloidal Fe_3O_4 as the core material instead of Fe_3O_4@SiO_2. TEM observation indicates that no polymers were formed on the surface Fe_3O_4 core (Fig. S5 in Supporting information). Such a result implies the silica shell with abundant silane groups are indispensable function in promoting the directional deposition of MF oligomers and MF/F127/TMB composite micelles.

To gain a deeper insight into the growth dynamics of mMF shell, small amounts of the reaction solution (0.5 mL) were withdrawn at different reaction intervals during the synthesis for transmission microscopy observation (Fig. S6 in Supporting information). TEM images (Figs. S6A-C) indicate that in the initial stage of the reaction, Fe_3O_4@SiO_2 cores were encapsulated by a dense layer of MF due to the rapid polymerization reaction of MF oligomers. The thickness of the MF layer grows to around 10 nm after 30 min. As the reaction further proceeded, a mesoporous structure gradually formed in the shell (Fig. S6D), indicating that MF/F127/TMB composite micelles gradually deposited. When the reaction time reached 120 min (Fig. S6E), the mesoporous shell became more pronounced due to the sufficient shell thickness. Due to the stress generated by intra/intermolecular interactions and the radial diffusion behavior of TMB in composite micelles, the spherical micelles gradually evolved into one-dimensional columnar micelles. After reaction for 180 min (Fig. S6F), the thickness of mesoporous shell remains almost unchanged, resulting in Fe_3O_4@SiO_2@mMF/F127 microspheres with radially aligned pore channels. By adjusting the concentration of HCl in the system, Fe_3O_4@SiO_2@mMF/F127 microspheres with spherical mesopores were also synthesized (Fig. S7 in Supporting information).

Based on the above results, a nanoemulsion-assisted interfacial assembly and polymerization mechanism was proposed for synthesizing Fe_3O_4@SiO_2@MF microspheres (Fig. 5). In the synthe-

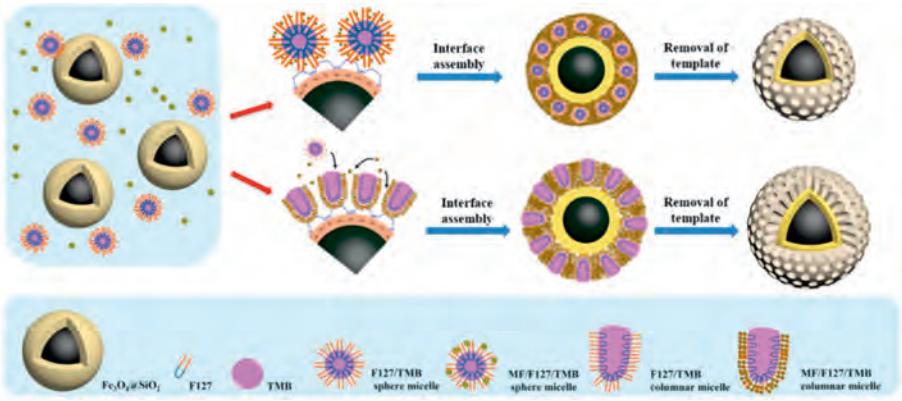


Fig. 5. Illustration of the formation mechanism for Fe_3O_4@SiO_2@mMF microspheres.

sis solution, the interaction between the hydrophilic headgroups of F127 and the acidic aqueous phase, along with the hydrophobic tails interacting with TMB, leading to the formation of uniform F127/TMB micelles. Next, pre-synthesized MF oligomers dissolved in the aqueous phase can interact with the F127/TMB micelles through the mediation of H^+, yielding MF/F127/TMB composite micelles. Due to the hydrogen bonding interaction between the amino groups of MF and silanol groups on the SiO_2 layer, MF/F127/TMB micelles can gradually deposit onto the surface of the pre-synthesized Fe_3O_4@SiO_2 microspheres as the reaction proceeded. The continuous condensation of MF oligomers increased the strength of the resin shell *via* enhancing crosslinking density. Therefore, during the final step of ethanol extraction of F127 and TMB, colloidal Fe_3O_4@SiO_2@mMF microspheres with a stable mesoporous polymer shell can be obtained. What is more, the mesoporous melamine-formaldehyde resin nanospheres were further synthesized in the same system in the absence of magnetic colloids to better illustrate the influence of magnetic silica core on the process of assembly and polymerization of mesostructured melamine-formaldehyde resin (Fig. S8 in Supporting information). This nanoemulsion-assisted interfacial assembly and polymerization method has significant potential for synthesizing a variety of core-shell mesoporous materials with diverse polymer shells, including amino phenolic resin and polydopamine. However, some key factors such as the polymer precursor selection, emulsion stability, and pore-forming mechanisms should be considered to achieve mesoporous nanocomposites with desired properties and structures. Further experimental exploration and optimization are required to fully realize the potential of this method for various applications.

In this study, by virtue of the useful superparamagnetism, large mesopores, abundant amino functional groups, the Fe_3O_4@SiO_2@mMF microspheres were further used as a unique platform for the facile and stable anchoring catalytically active heteropoly acids (HPAs) through salt-forming reactions between the amino groups and HPAs. HPAs, distinguished by their high acidity and redox capability, are widely studied in various fields, including heterogeneous catalysis [60–62], photocatalysis [63,64], electrochemistry [65–67] and antibacterial applications. In this study, we reported the successful immobilization of PTA, a typical HPA, within the pore channels of Fe_3O_4@SiO_2@MF microspheres. Subsequently, the catalytic performance of the novel heterogeneous catalysts was evaluated in the esterification reaction between butanol and acetic acid. Moreover, the antibacterial efficacy of the supported PTA against *E. coli* and *S. aureus* was examined.

TEM images demonstrate that Fe_3O_4@SiO_2@mMF/PTA microspheres maintain the morphology after loading PTA (Figs. S9, S10A and B in Supporting information), and compared with the microspheres before loading PTA (Fig. 2), the pore channels became less pronounced due to the strong interaction of PTA and the mMF shell, confirming the stable immobilization of PTA. The elemental mapping (Figs. S10C-J in Supporting information) and EDX (Fig. S10K in Supporting information) revealed the three-layered structure of the composite microspheres and confirmed their high loading capacity for PTA, with P and W elements accounting for 0.3 wt% and 11.4 wt%, respectively. Furthermore, the FTIR spectroscopy characterization (Fig. S11 in Supporting information), zeta potential measurement (Fig. S12 in Supporting information) and XPS analysis (Fig. S13 in Supporting information) provided additional evidence that confirmed the successful loading of PTA onto Fe_3O_4@SiO_2@mMF microspheres.

To assess the catalytic performance of Fe_3O_4@SiO_2@mMF/PTA, an esterification reaction between acetic acid and butanol was conducted under 120 °C, with detailed product analysis conducted *via* gas chromatography-mass spectroscopy (GC–MS) (Fig. S14 in Supporting information). The definitive detection of acetic acid ($m/z = 60$, retention time (RT) = 1.95 min), butanol ($m/z = 74$, RT = 2.13 min), and the primary product butyl acetate ($m/z = 116$, RT = 3.14 min) confirms the successful esterification process. Temporal monitoring of the reaction kinetics (Fig. S14E in Supporting information) reveals an initially rapid reaction rate, which gradually decelerated owing to the inhibitory effect of accumulating butyl acetate. After reacting for 8 h, the conversion of acetic acid reached 92 %, indicative of a high activity of the catalyst. Moreover, the convenient separation and purification by a magnet (~2000 Gauss) facilitate the reuse of Fe_3O_4@SiO_2@mMF/PTA catalyst. As depicted in Fig. S15 (Supporting information), the conversion rate of acetic acid remains above 88 % even after 10 cycles for reuse, indicating its excellent recyclability and vast potential for applications in esterification and other organic transformations. TEM characterization of the recycled catalysts (Fig. S16 in Supporting information) revealed the well-remained structure and morphology, indicating a good stability of the catalyst. The antibacterial potential of Fe_3O_4@SiO_2@mMF/PTA against both Gram-positive bacteria *S. aureus* and Gram-negative bacteria *E. coli* was evaluated qualitatively and quantitatively by the colony counting method ($n = 4$) (Fig. S17 in Supporting information). The viability rates for *S. aureus* were 50.15 %, 27.09 %, 11.58 %, and the viability rates for *E. coli* were 57.41 %, 29.28 %, 7.35 % in the PTA-1, PTA-2, and PTA-3 groups with increasing Fe_3O_4@SiO_2@mMF/PTA concentrations, respectively. These results above demonstrate a clear and positive correlation between the Fe_3O_4@SiO_2@mMF/PTA concentration and the antibacterial efficacy. In comparison, in the PTA-0 groups with the same concentration of Fe_3O_4@SiO_2@mMF as PTA-3 but without PTA, the viability rates for *S. aureus* and *E.*

coli are only 65.89 % and 76.06 %, respectively, which confirm the remarkably better antibacterial efficacy of Fe_3O_4@SiO_2@mMF/PTA against the both bacteria. What is more, the structure and morphology of Fe_3O_4@SiO_2@mMF/PTA microspheres remain intact after antibacterial application, which underscores the excellent stability of the PTA-loaded microspheres (Fig. S18 in Supporting information). Such a superior performance can be attributed to the superchaostropic nature of PTA, which acts as a "nanohunter" capable of arousing special effects and biological interactions with bacterial strains. According to the Hofmeister Series, the PTA species with low polarity and nanoscale can facilitate cell wall protein denaturation and unfolding, thus inducing the "salting-in" effect, cell wall disruption, and subsequent leakage of intracellular material [68]. The compromised cell wall allows the water-soluble and highly redox-active PTA to penetrate the cellular compartment, directly oxidizing proteins, lipids, and other bacterial substances, causing fatal damage to bacterial cells [69–72]. Additionally, Fe_3O_4@SiO_2@mMF, with its high surface area and open pores, serves as an ideal carrier, facilitating an enhanced reaction area and efficient PTA loading. This, in turn, accelerates the antibacterial process and effectively inhibits bacterial growth, further underscoring the potential of Fe_3O_4@SiO_2@mMF/PTA as a powerful antibacterial agent. What is more, taking *E. coli* as an example, the protein content in the broth was quantified using the bicinchoninic acid (BCA) assay to assess the leakage of cellular contents (Fig. S19 in Supporting information). The results revealed a notable elevation in protein levels within the PTA-0, PTA-1, PTA-2, and PTA-3 treatment groups compared to the control group, further confirming the antibacterial mechanism of the microspheres.

In conclusion, core-multishell magnetic mesoporous melamine-formaldehyde resin microspheres (Fe_3O_4@SiO_2@mMF) are successfully fabricated *via* a nanoemulsion-assisted interfacial co-assembly and polymerization approach. The resulting Fe_3O_4@SiO_2@mMF microspheres exhibit radially accessible mesopores, superparamagnetic responsiveness, and abundant active sites. Upon PTA loading, Fe_3O_4@SiO_2@mMF/PTA demonstrates excellent antimicrobial performance against *S. aureus* and *E. coli* (with viabilities of 11.58 % and 7.35 %, respectively), alongside remarkable heterogeneous catalytic activity (conversion over 90 %) and recyclability in the esterification of *n*-butanol with acetic acid. This work not only paves a promising path for developing highly efficient and environmentally friendly heterogeneous catalysts but also opens avenues for future research exploring the versatile utility of these microspheres in chemical transformations, biomedicine, and targeted drug delivery systems.

Declaration of competing interest

The authors declare that they have no known competing financial interests or personal relationships that could have appeared to influence the work reported in this paper.

CRediT authorship contribution statement

Jiarong Li: Writing – review & editing, Writing – original draft, Investigation, Data curation. **Shude Liu:** Writing – review & editing, Writing – original draft, Investigation, Data curation. **Yuanzhao Xie:** Writing – original draft, Investigation. **Yue Sun:** Writing – review & editing, Writing – original draft. **Zhuyu Liu:** Writing – original draft, Validation. **Meihua Chen:** Writing – original draft, Funding acquisition. **Yaobang Li:** Writing – original draft, Project administration, Funding acquisition. **Yonghui Deng:** Writing – review & editing, Writing – original draft, Supervision, Project administration, Funding acquisition, Conceptualization.

Acknowledgments

This work was financially supported by National Key R&D Program of China (No. 2024YFD2402203), National Natural Science Foundation of China (Nos. 22125501, U22A20152), Science and Technology Commission of Shanghai Municipality (No. 2024ZDSYS02).

Supplementary materials

Supplementary material associated with this article can be found, in the online version, at doi:10.1016/j.cclet.2025.111433.

References

[1] J. Liu, X. Chen, K. Chen, et al., Science 383 (2024) 1198–1204.
[2] E.J.W. Crossland, N. Noel, V. Sivaram, et al., Nature 495 (2013) 215–219.
[3] W. Xie, X. Huang, C. Zhu, et al., Adv. Mater. 36 (2024) 2313920.
[4] Q. Yuan, A.X. Yin, C. Luo, et al., J. Am. Chem. Soc. 130 (2008) 3465–3472.
[5] Y. Liang, X. Yang, X. Wang, et al., Nat. Commun. 14 (2023) 5223.
[6] Y. Kang, S. Li, O. Cretu, et al., Sci. Adv. 10 (2024) eado2442.
[7] M. Eguílaz, R. Villalonga, G. Rivas, Biosens. Bioelectron. 111 (2018) 144–151.
[8] Z. Tang, X. Li, L. Tong, et al., Angew. Chem. Int. Ed. 133 (2021) 23800–23805.
[9] F. Jiang, Y. Deng, K. Chen, et al., Adv. Mater. 36 (2024) 2313547.
[10] Y. Ren, Y. Deng, Z. Wang, et al., Small 20 (2024) 2311659.
[11] T. Zhao, L. Chen, M. Liu, et al., Nat. Chem. 15 (2023) 832–840.
[12] X. Hong, X. Zhong, G. Du, et al., Sci. Adv. 6 (2020) eaaz4462.
[13] S. Liu, J. Li, Y. Zou, et al., Small 19 (2023) 2304631.
[14] X. Huang, J. Gao, Y. Qin, et al., ACS Nano 18 (2024) 21459–21471.
[15] G.O. Park, J. Yoon, S.B. Park, et al., Small 14 (2018) 1702985.
[16] J. Liu, T. Yang, D.W. Wang, et al., Nat. Commun. 4 (2013) 2798.
[17] T. Zhao, X. Zhang, R. Lin, et al., J. Am. Chem. Soc. 142 (2020) 20359–20367.
[18] Y. Li, B.P. Bastakoti, M. Imura, et al., Chem. Eur. J. 21 (2015) 6375–6380.
[19] D. Niu, Z. Liu, Y. Li, et al., Adv. Mater. 26 (2014) 4947–4953.
[20] D. Shen, J. Yang, X. Li, et al., Nano Lett. 14 (2014) 923–932.
[21] Z. Teng, S. Wang, X. Su, et al., Adv. Mater. 26 (2014) 3741–3747.
[22] S. Kerkhofs, T. Willhammar, H. Van Den Noortgate, et al., Chem. Mater. 27 (2015) 5161–5169.
[23] Y. Meng, D. Gu, F. Zhang, et al., Chem. Mater. 18 (2006) 4447–4464.
[24] F. Wei, T. Zhang, R. Dong, et al., Nat. Protoc. 18 (2023) 2459–2484.
[25] L. Peng, H. Peng, W. Li, et al., Nat. Protoc. 18 (2023) 1155–1178.
[26] P. Zhang, L. Wang, S. Yang, et al., Nat. Commun. 8 (2017) 15020.
[27] X. Yang, P. Lu, L. Yu, et al., Adv. Funct. Mater. 30 (2020) 2002488.
[28] R. Mo, F. Li, X. Tan, et al., Nat. Commun. 10 (2019) 1474.
[29] C. Cui, W. Qian, Y. Yu, et al., J. Am. Chem. Soc. 136 (2014) 2256–2259.
[30] S.T. Lim, J.H. Kim, C.Y. Lee, et al., Sci. Rep. 9 (2019) 10922.
[31] X. Zhu, Y. Xia, X. Zhang, et al., J. Mater. Chem. A 7 (2019) 8975–8983.
[32] P. Liu, Y. Li, C. Sun, et al., ACS Appl. Nano Mater. 8 (2025) 7267–7277.
[33] M. Lei, M. Gao, X. Yang, et al., ACS Appl. Mater. Interfaces 13 (2021) 51933–51944.
[34] J. Ma, Y. Li, X. Zhou, et al., Small 16 (2020) 2004772.
[35] F. Ma, Y. Yang, G. Jiao, et al., RSC Adv. 14 (2024) 25227–25234.
[36] J. Liu, M. Zheng, X. Shi, et al., Adv. Funct. Mater. 26 (2016) 919–930.
[37] D. Wang, T. Xie, Q. Peng, et al., J. Am. Chem. Soc. 130 (2008) 4016–4022.
[38] H. Huang, S. Yin, Z. Fu, et al., J. Mater. Chem. C 18 (2025) 9106–9114.
[39] J. Kim, H.S. Kim, N. Lee, et al., Angew. Chem. Int. Ed. 47 (2008) 8438–8441.
[40] Y. Deng, D. Qi, C. Deng, et al., J. Am. Chem. Soc. 130 (2008) 28–29.
[41] Y. Deng, Y. Cai, Z. Sun, et al., J. Am. Chem. Soc. 132 (2010) 8466–8473.
[42] H. Yi, Y.F. Zhao, Y.T. Chan, et al., Science 383 (2024) 634–639.
[43] M. Urso, M. Ussia, X. Peng, et al., Nat. Commun. 14 (2023) 6969.
[44] Y. Zou, Z. Sun, Q. Wang, et al., Chem. Rev. 125 (2025) 972–1048.
[45] Z. Zhang, P. He, W. Ma, et al., Adv. Funct. Mater. 33 (2023) 2302212.
[46] Q. Yue, J. Li, Y. Zhang, et al., J. Am. Chem. Soc. 139 (2017) 15486–15493.
[47] Y. Zhang, Q. Yue, L. Yu, et al., Adv. Mater. 30 (2018) 1800345.
[48] J. Zhang, W. Sun, L. Bergman, et al., Mater. Lett. 67 (2012) 379–382.
[49] R. de Andrade, R.d.C.d.R. Schmidt, L.S. Gomes, et al., Pharmaceutics 16 (2024) 357.
[50] Y. Zhang, Q. Yue, M.M. Zagho, et al., ACS Appl. Mater. Interfaces 11 (2019) 10356–10363.
[51] P. Pan, Q. Yue, X. Yang, et al., Small 17 (2021) 2006925.
[52] H. He, S. Ye, W. Zhang, et al., Chem. Eng. J. 489 (2024) 151294.
[53] J. Li, S. Liu, Y. Xie, et al., J. Mater. Chem. A 12 (2024) 22627–22636.
[54] Y. Liu, S. Wu, W. Xiong, et al., Adv. Mater. Interfaces 10 (2023) 2201631.
[55] D. Wu, J. Zhou, X. Chen, et al., Biomaterials 238 (2020) 119847.
[56] S. Gao, Z. Wang, L. Ma, et al., ACS Catal. 10 (2020) 1375–1380.
[57] Z. Xiao, W. Zuo, L. Chen, et al., ACS Appl. Mater. Interfaces 13 (2021) 43925–43936.
[58] J. Liu, Z. Sun, Y. Deng, et al., Angew. Chem. Int. Ed. 48 (2009) 5875–5879.
[59] H.L. Ding, Y.X. Zhang, S. Wang, et al., Chem. Mater. 24 (2012) 4572–4580.
[60] I.D. Ivanchikova, N.V. Maksimchuk, R.I. Maksimovskaya, et al., ACS Catal. 4 (2014) 2706–2713.

[61] L. Hombach, N. Hausen, A.G. Manjón, et al., Appl. Catal. A: Gen. 666 (2023) 119392.
[62] X.Y. Xue, Y. Sun, Q.W. Sun, et al., Sustain. Energy Fuels 8 (2024) 1295–1303.
[63] N.I. Gumerova, A. Rompel, Nat. Rev. Chem. 2 (2018) 0112.
[64] T. Li, J.D. Cui, L.M. Gao, et al., ACS Sustain. Chem. Eng. 8 (2020) 13352–13361.
[65] G.Y. Ryu, H. Jae, K.J. Kim, et al., ACS Appl. Energy Mater. 6 (2023) 4283–4296.
[66] S. Mukhopadhyay, J. Debgupta, C. Singh, et al., Angew. Chem. Int. Ed. 57 (2018) 1918–1923.
[67] Y. Liu, S. Liu, X. Lai, et al., Adv. Funct. Mater. 25 (2015) 4480–4485.
[68] B. Kang, H. Tang, Z. Zhao, et al., ACS Omega 5 (2020) 6229–6239.
[69] Y. Fang, C. Xing, S. Zhan, et al., J. Mater. Chem. B 7 (2019) 1933–1944.
[70] S.S. Soares, H. Martins, R.O. Duarte, et al., J. Inorg. Biochem. 101 (2007) 80–88.
[71] M. Aureliano, Oxid. Med. Cell. Longev. 2016 (2016) 6103457.
[72] D. Chang, Y. Li, Y. Chen, et al., Nanoscale Adv. 4 (2022) 3689–3706.